# Tricontinuous Cubic Nanostructure and Pore Size Patterning in Mesostructured Silica Films Templated with Glycerol Monooleate

Darren R. Dunphy,[†] Fred L. Garcia,[†] Bryan Kaehr,[†,‡] Constantine Y. Khripin,[⊥] Andrew D. Collord,[‡] Helen K. Baca,[†] Michael P. Tate,[#] Hugh W. Hillhouse,[§] Joseph W. Strzalka,[‖] Zhang Jiang,[‖] Jin Wang,[‖] and C. Jeffrey Brinker*,[†,‡]

[†]University of New Mexico/NSF Center for Micro-Engineered Materials, Department of Chemical and Nuclear Engineering, Albuquerque, New Mexico 87131, United States

[‡]Advanced Materials Laboratory, Sandia National Laboratories, Albuquerque, New Mexico 87106, United States

[§]Department of Chemical Engineering, University of Washington, Seattle, Washington 98195, United States

[‖]Advanced Photon Source, Argonne National Laboratory, Argonne, Illinois 60439, United States

Ⓢ Supporting Information

ABSTRACT: The fabrication of nanostructured silica films possessing tricontinuous minimal surface mesophases with well-defined framework and pore connectivity remains a difficult task. As a new route to these structures, we introduce glycerol monooleate (GMO) as a template for evaporation-induced self-assembly. As deposited, a nanostructured double gyroid phase is formed, as indicated by analysis of grazing-incidence small-angle X-ray scattering data. Removal of GMO by UV/O_3 treatment or acid extraction induces a phase change

to a nanoporous body-centered structure, which we tentatively identify as based on the IW-P surface. To improve film quality, we add a cosurfactant to the GMO in a mass ratio of 1:10; when this cosurfactant is cetyltrimethylammonium bromide, we find an unusually large pore size (8—12 nm) in acid extracted films, while UV/O_3 treated films yield pores of only about 4 nm. Using this pore size dependence on the film processing procedure, we create a simple method for patterning pore size in nanoporous films, demonstrating spatially defined size-selective molecular adsorption.

KEYWORDS: evaporation-induced self-assembly, porous films, tricontinuous phases, gyroid, glycerol monooleate, grazing-incidence small-angle X-ray scattering, film patterning
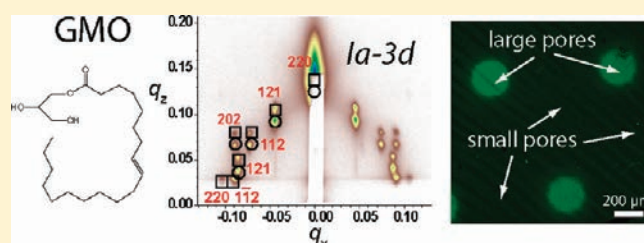
Evaporation-induced self-assembly (EISA)[1,2] has enabled the rapid synthesis of a wide range of nanostructured thin-film materials through the coassembly of inorganic or hybrid molecular precursors around extended liquid crystalline mesophases obtained from amphiphilic structure-directing agents (SDAs). Easily accessible nanostructure morphologies obtainable through EISA include lamellar, 2-D hexagonal, and 3-D cubic or hexagonal phases formed via packing of SDA micelles. However, the EISA synthesis of tricontinuous 3-D architectures formed through draping an SDA bilayer over a minimal surface (exemplified by $Ia3d$ "double gyroid", $Im3m$ "plumber's nightmare" or IW-P, and $Pn3m$ "double diamond" structures) has proven to be a challenge for thin films in comparison to synthesis of these structures in powdered materials,[3] presumably a consequence of rapid self-assembly kinetics. These phases, in particular the double gyroid, are characterized by well-defined 3-D pore and framework connectivity with desirable transport properties throughout the pore network[4] and are of interest for applications including nanostructured membranes, sensors, and photovoltaic devices.[5,6] Previous synthetic routes to mesostructured and mesoporous oxide films with double gyroid structure

include thermal annealing of predeposited films templated with the nonionic surfactant Brij 56,[7] use of a polymeric poly(ethylene oxide)-poly(propylene oxide)-alkane surfactant,[8] and assembly of block copolymers, followed by the sacrificial removal of one polymer component and subsequent infiltration of an oxide material.[9] Recently, an EISA synthesis of the double gyroid structure was reported using the Pluronic block copolymer P84.[10] Unfortunately, these routes to double gyroid films are challenging in practice, very sensitive to experimental conditions, or rely on noncommercially available SDAs, driving a need for new, experimentally convenient routes to films with tricontinuous nanostructure morphology.

We hypothesized that use of the lipid glycerol monooleate (GMO, structure given in Figure 1A) as an SDA for EISA would provide a practical route to tricontinuous minimal surface-type mesophases in thin silica films; GMO is well-known for structural diversity in GMO/H_2O phase diagrams that include regions of $Ia3d$, $Im3m$, and $Pn3m$ symmetry.[11,12] In EISA-derived silica
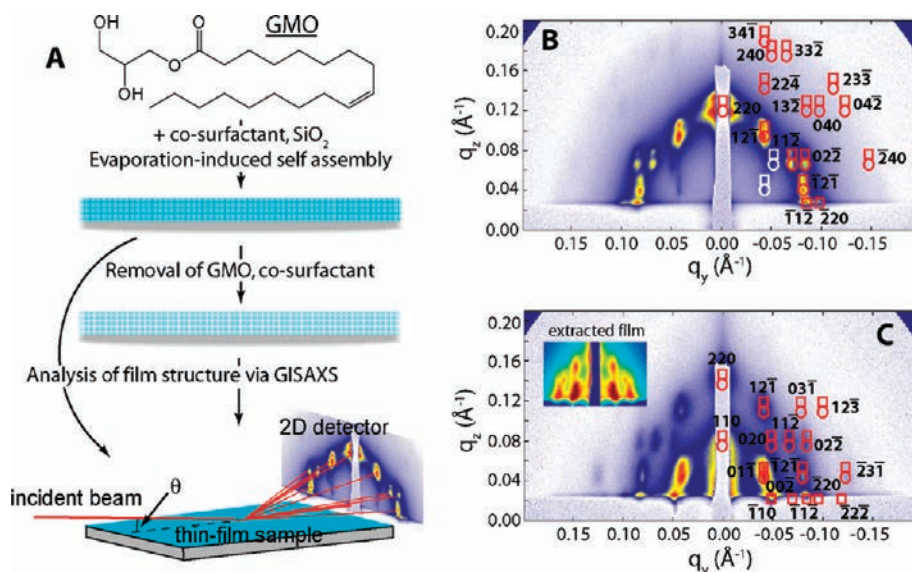
Figure 1. (A) Structure of GMO and general procedure for fabrication and analysis of nanoporous films using this template and (B) and (C) GISAXS data for GMO/diC_6PC-templated silica films. (B) As deposited, indexed to space group $Ia3d$ (double gyroid). Circles and squares indicate the predicted positions of scattering arising from the direct and reflected beams, respectively. White signifies the position of normally forbidden reflections for this space group. (C) After removal of the template by UV/O_3 treatment, indexed to space group $Im3m$. The inset contains GISAXS data for an acid-extracted film, also showing an $Im3m$ nanostructure.

films, we find that GMO does indeed form an $Ia3d$ phase, with a phase transformation to $Im3m$ upon removal of GMO by UV/O_3 treatment or solvent extraction. Although $Im3m$ can describe a body-centered cubic packing of micelles, we tentatively assign this phase to a minimal surface structure (I-WP) on the basis of TEM data as well as pore size and unit cell dimensions. We also note two unusual properties of GMO-templated films not observed previously in nanoporous films synthesized through self-assembly: large pore sizes (up to 10−12 nm) typical of films, templated with polymeric templates but here obtained with a small-molecule SDA, and a dependence of pore size on GMO removal procedure, enabling the patterning of pore size over macroscopic scales using a simple procedure.

GMO/silica films were synthesized using a similar procedure as that previously described for phospholipid/silica films,[13,14] with the exception that a cosurfactant was added to the precursor sol in a 1:10 cosurfactant/GMO mass ratio in order to improve both the macroscopic and nanoscale quality of the resulting films (Figure 1A). For cosurfactants, we investigated both synthetic amphiphiles, including cetyltrimethylammonium bromide (CTAB) and Brij 56, as well as other lipids (dihexyl phosphatidylcholine, egg lecithin, lyso phosphatidylcholines with 10−16 carbon tails, and the bile salt derivative sodium taurodeoxycholate), finding that film optical quality was increased when compared to films synthesized without a cosurfactant, while enhancing the overall nanoscale order as observed by grazing-incidence small-angle X-ray scattering (GISAXS)[8,13,15] (see Supporting Information). Because the cosurfactant dihexyl phosphatidylcholine (diC_6PC) was found to produce the highest quality nanostructure, our characterization efforts were focused on GMO/ diC_6PC-templated films. GISAXS was used as the primary means of nanostructure analysis; unlike transmission electron microscopy (TEM), GISAXS interrogates the overall nanostructure of the film. In this technique, a beam is reflected from the film/substrate interface at an incident angle greater than the critical angle of the film but less than that of the substrate,

maximizing the interaction volume between X-rays and film.[16] Panel (B) of Figure 1 shows a typical GISAXS pattern for a GMO/diC_6PC/silica film before template removal, indexed to cubic space group $Ia3d$ oriented with the [110] axis perpendicular to the substrate and a lattice parameter of a = 17.8 nm, contracted by 14% along the surface normal due to drying stresses during film self-assembly. The scattering pattern was simulated using NANOCELL,[15] taking into account the effects of reflection and refraction within the film. The space group $Ia3d$ is consistent with a tricontinuous mesophase derived from the minimal G (double gyroid) surface. Two sets of reflections normally forbidden to $Ia3d$ ((020), (1−10)) are also present in this GISAXS data; however, after contraction of $Ia3d$ along one axis, both {110} and {200} planes may be observed due to distortions of mesophase symmetry.[8,17] TEM analysis is also consistent with the assignment of the mesophase to a [110]-oriented double gyroid. Panel (A) of Figure 2 shows a typical plan view image we assign to the (110) plane parallel to the substrate surface, supported by similarity to simulated data[8] as well as indexing of the image Fourier transform (panel C).

Panel (C) of Figure 1 contains GISAXS data for the same film after template removal by UV/O_3 exposure[18] for 30 min, showing the appearance of strong {110} and {200} reflections that we attribute to a phase change from $Ia3d$ to a [110]-oriented $Im3m$ mesostructure (a = 18.5 nm, contracted 32% along [110]). Although the strengthening of these reflections over that shown in panel (B) of Figure 1 could result from further distortion of the $Ia3d$ phase, we note that (1) unlike previous reports of this distortion, {110} reflections are much more intense than the allowed reflections for $Ia3d$, and more importantly, (2) TEM plan views (Figure 2B) indexed Fourier transform for this image in panel C show the presence of regions identifiable as the (110) view of $Im3m$ with the above lattice parameters. However, because TEM analysis also shows other areas consistent with the (110) view of $Ia3d$, we posit that a mixed $Ia3d$/$Im3m$ phase is present. The space group $Im3m$ corresponds to a body-centered
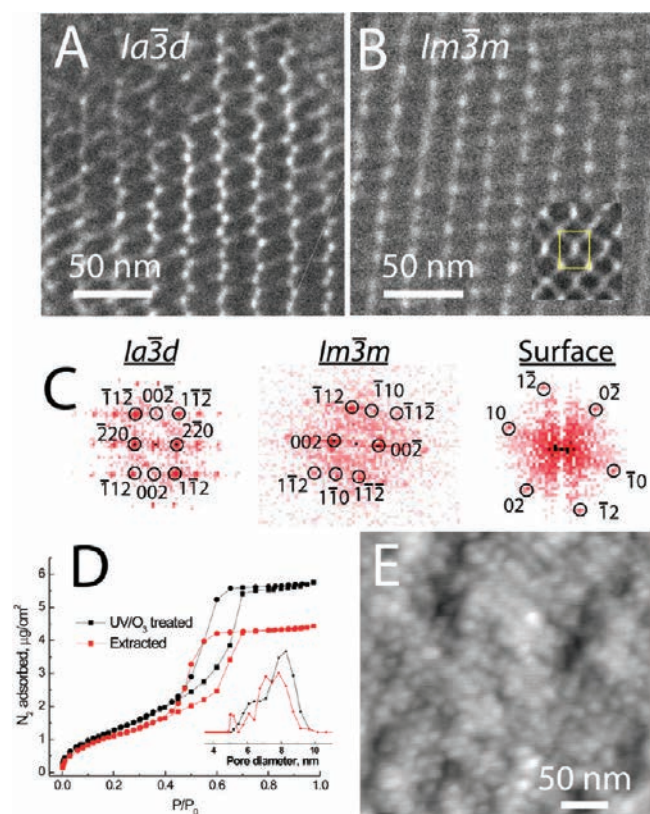
Figure 2. (A) Plan view TEM image of the same film as analyzed in panel (B) of Figure 1, consistent with the (220) plane of the double gyroid structure. (B) Plan view TEM image of the same film as analyzed in panel (C) of Figure 1, consistent with the (110) plane of a body-centered cubic structure. The inset highlights the nanostructure unit cell (scale reduced in inset by 33%). (C) 2-D Fourier transforms for data in panels (A), (B), and (E), respectively. (D) N_2 adsorption isotherms for GMO/diC_6PC-templated silica films after UV/O_3 treatment and acid extraction, along with an inset showing pore size distributions calculated from the adsorption branch of these isotherms. (E) AFM image of the same film as analyzed in panel (C) of Figure 1, showing a regular surface patterning consistent with the TEM data in panel (B).

cubic unit cell, describing either a phase formed by packing of discrete micelles[19] or a phase based on a bicontinuous surface (candidates here include the so-called "plumber's nightmare" P-surface,[17] as well as the higher genus I-WP surface). In addition to UV/O_3 treatment, room temperature extraction in 0.1 M HCl in ethanol also induced the same transition to $Im\bar{3}m$ (inset, Figure 1C); unit cell parameters for the extracted film are about 20% greater than for the UV/O_3 treated film, although the film also experiences approximately 25% more shrinkage in the direction normal to the substrate surface.

Nitrogen physisorption data for a UV/O_3 treated GMO/diC_6PC/silica film is shown in panel (D) of Figure 2, obtained on a 220 nm thick film using a surface acoustic wave (SAW) technique.[20] The total film porosity calculated from this data is 31%, a value consistent with that obtained from spectroscopic ellipsometry (30%), indicating that the entire internal pore volume is connected and accessible to the film surface; however, the hysteresis seen in the desorption branch of the isotherm does signify the presence of a significant "bottleneck" inside the pore structure. An estimated pore size distribution (PSD), calculated from the adsorption branch of the N_2 isotherm using a hybrid

DFT model for SiO_2 with cylindrical pores incorporating experimental pore size data of MCM-41 type materials as well as statistical mechanical simulations,[21] is shown as an inset. Comparison of our results using this DFT model with classical methods of PSD determination (e.g., Barrett, Joyner, and Halenda calculations using the statistical film thickness curve of Kruk, Jaroniec, and Sayari, commonly abbreviated as BJH-KJS)[22] shows a close agreement of average pore size (about 0.6 nm for 5 nm pores); the DFT method was selected as the method of analysis primarily for the improved number of data points in the PSD at higher pore size relative to BJH methods. We note that, more than the exact type of model used to calculate the PSD, the use of a model for cylindrical pores is likely a greater source of error. However, the exact pore morphology in these GMO-templated films is not known, and relative errors in PSD calculations do not modify any conclusions of this report (bimodality of pore size, unusually large pore size relative to what is expected for templating by a GMO micelle or bilayer.) The PSD has two notable features: bimodality and an unusually large average pore size for small-molecule SDAs (about 8 nm, consistent with TEM observation). While the bimodal PSD may be due to differential pore size between the $Ia\bar{3}d$ and $Im\bar{3}m$ phases, the PSD should be similar for all mesophase structures for a given amphiphilic SDA, approximately equal to two molecular lengths (the thickness of a bilayer or diameter of a spherical micelle), about 4 nm for GMO. Panel (D) of Figure 2 also contains N_2 adsorption and calculated PSD for an acid/ethanol extracted film. Although the unit cell dimensions of extracted films were found to be larger than for UV/O_3 processed films, the PSD is nearly identical, with a lower total accessible porosity possibly arising from a combination of film shrinkage and incomplete extraction of the template from the pore network.

AFM analysis using a sharp silicon cantilever (2 nm tip radius) was used to investigate the surface topography of GMO-templated silica films as a means of developing further insight into the internal structure of these materials.[23,24] Panel (E) of Figure 2 contains a height image for the same film as analyzed in panel (C) of Figure 1 and panel (B) of Figure 2, showing a periodic array of rectangular mounds with heights of 1−2 nm and lattice dimensions of about 15−20 nm. Fourier analysis of this image (Figure 2C) yields a pattern that we index to the plane group *pmm*, consistent with the (110) plane of the $Im\bar{3}m$ nanostructure fit to the GISAXS data in panel (C) of Figure 1. Long-range data (Supporting Information) shows the extension of this topology across the entire film surface, with domain size of about 200−500 nm, as well as 40 ± 2 nm deep chasms at domain boundaries. This mound-like surface topology is not present before template removal, supporting the assignment of the {110} and {002} features in panel (C) of Figure 1 to a new phase rather than to a manifestation of nanostructure distortion.

Although the specific structure of the $Im\bar{3}m$ phase is not known, we tentatively assign a minimal surface type nanostructure on the basis of three observations. First, N_2 physisorption shows the presence of a well-connected pore network, but with pore diameters (about 8−10 nm) less than that needed for the formation of a continuous pore volume in body-centered packing of spherical micelles given the large unit cell parameters (a = 18.5 nm by GISAXS). Also, TEM images of the (110) plane (Figure 2B) show a unit cell consisting of interconnected nodes rather than close-packed spherical voids.[25] Finally, noting that 8 nm features should be resolvable with the AFM tips used in the analysis of surface topology (tip diameter = 2 nm), we do not

observe spherical pore openings at the surface of the film[23] but rather rectangular features consistent with channel-like pores arranged in a rectangular lattice. Although the precise assignment of the pore network structure will require further analysis, on the basis of the body-centered lattice (Figure 1C), lattice orientation ([110] perpendicular to the substrate), and network connectivity within the unit cell (Figure 2B, body center to unit cell vertices), we posit a mesophase based upon the I-WP surface (Figure 3). Furthermore, we hypothesize that the large pore size measured by N_2 adsorption data, equal to twice the bilayer thickness of GMO, is a result of a unique property of the I-WP surface; unlike the G or D surfaces, the I-WP does not bisect two equivalent volumes, differing in network coordination (8-fold vs 4-fold) as

Figure 3. IW-P surface, posited as the structural element for the nanostructure of GMO-templated films after UV/O_3 treatment or acid extraction. Yellow and red signify interior volumes with 8-fold and 4-fold connectivity, respectively.

well as relative volume. If the inner phase is unstable toward GMO removal, collapse of this volume would merge adjacent surfaces, resulting in a pore size equal to the thickness of two GMO bilayers.

GMO films synthesized with other cosurfactants were found to exhibit identical behavior with respect to film nanostructure and pore size distribution. However, the pore size distribution of films using CTAB as the cosurfactant were found to be dependent on the method of template removal (Figure 4A,B). Unlike films made with other cosurfactants, GMO/CTAB films processed with UV/O_3 exposure yielded average pore sizes of only about 4.5 nm as measured by N_2 adsorption, consistent with one bilayer thickness of GMO. Also, template extraction yielded an average pore sizes of about 12 nm, significantly larger than that seen in GMO-templated films synthesized with other cosurfactants. Although the source of this processing-dependent pore size distribution is unknown, we note that the GISAXS scattering patterns for GMO/CTAB/SiO_2 films (Supporting Information) are qualitatively similar to those of GMO/diC$_6$PC/SiO_2 films, suggesting that differences in mesophase type are not likely the source of this property. Within the context of our hypothesized mechanism for the origin of the large pore size in GMO/diC$_6$PC-templated films, it is possible that the presence of CTAB modifies the stability of the inner I-WP volume, stabilizing the mesophase toward template removal by UV/O_3 treatment. The 12 nm pore size in extracted films may also be an effect of mesophase distortion/swelling by CTAB (although in films processed through a sequential masked UV/extraction procedure, the pore size is only 8 nm in extracted regions, as seen in GMO/ diC$_6$PC films; see below).
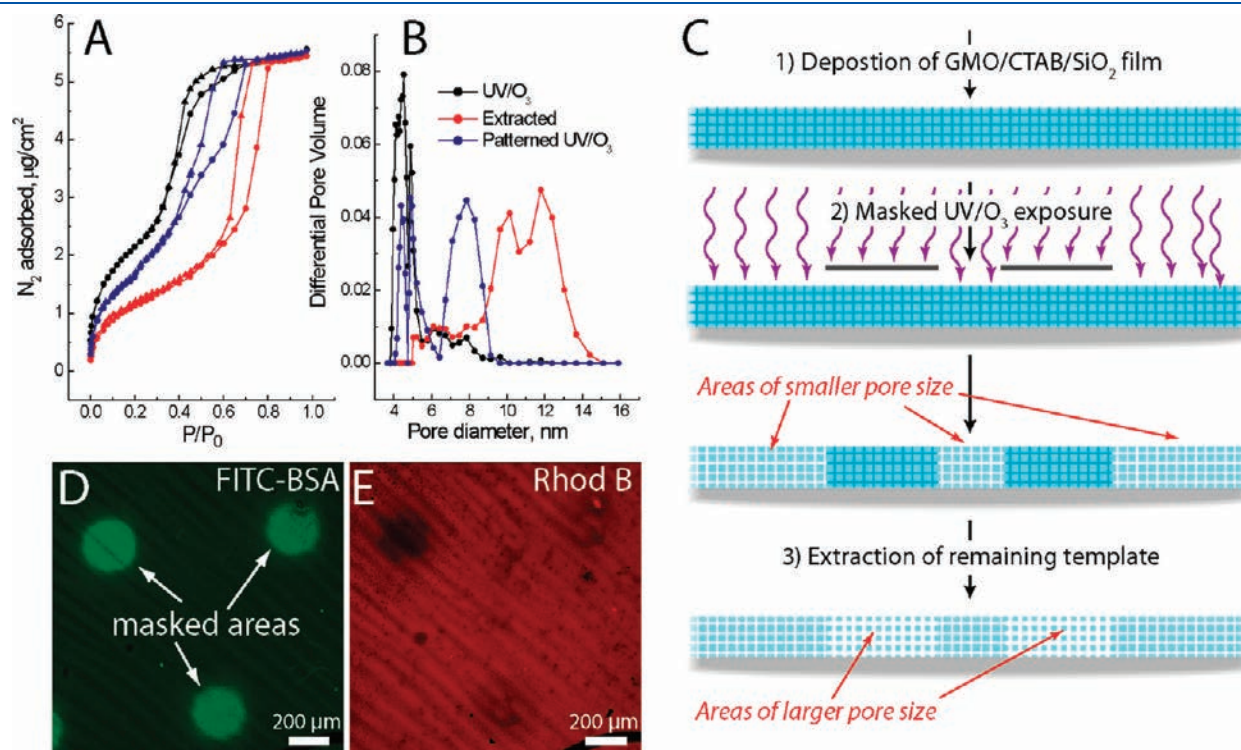

Figure 4. (A) N_2 adsorption isotherms of GMO/CTAB-templated silica films after acid extraction, UV/O_3 treatment, and a combined UV/O_3/extraction patterning process. (B) Pore size distributions calculated from adsorption branches of the data in panel A. (C) Procedure for optical patterning of pore size in GMO/CTAB-templated films. (D,E) Fluorescent microscopy of a GMO/CTAB-templated silica film after pore size patterning, showing the (D) adsorption of fluorescently labeled protein (BSA) only in regions that were masked during UV/O_3 processing, forming about 8 nm pores during the subsequent acid extraction, with all film regions accessible to the small molecule rhodamine B (panel E).

Using the pore size dependence on postsynthesis film processing in the GMO/CTAB/SiO$_2$ system, we have developed a straightforward approach to optically pattern pore size in nanoporous films, as illustrated in panel (C) of Figure 4. Although other film properties have been patterned (for example, film nanostructure[26]), this is, to the best of our knowledge, the first observation of optically definable pore size in nanoporous membranes. In our approach, the as-deposited film is first exposed to UV/O$_3$, using a metallized optical mask to protect regions where larger pore size is desired. After UV/O$_3$ treatment, the entire film is extracted in acidified ethanol; the areas of the film that have template removed by UV/O$_3$ treatment produce regions of small (about 4 nm) pores, while masked areas, where GMO is removed by the subsequent extraction step, yield regions of significantly larger pores. Panels (A) and (B) of Figure 4 contain a N$_2$ adsorption isotherm obtained for a film patterned in this manner, along with a calculated PSD. Clearly, the PSD is bimodal, with one distribution between 4 and 5 nm, identical to that seen in the data for a UV/O$_3$ treated film, and the other with an average pore size of about 7−8 nm. As noted previously, this size is significantly less than that shown in the data for a film processed only by extraction; although this may be an effect of mesophase distortion, the exact source of this difference in pore dimensions is a topic of future investigation.

Panels (D) and (E) of Figure 4 demonstrate how this patterning process can be used to localize molecular elements based upon physical size. A patterned film was immersed in a solution containing both rhodamine B (a small-molecule fluorophore with dimensions of about 1 nm) and fluorescein isothyocynate-labeled bovine serum albumen (FITC-BSA, about 5−6 nm in diameter). As shown in panel D, FITC-BSA largely adsorbs into regions of the film that had been masked during the UV/O$_3$ treatment step; the fluorescent signal of these regions is at least 8-fold greater than that of the nonmasked areas. However, rhodamine B is adsorbed into the film in all regions. Control experiments on nonextracted samples show that this effect is not due to surface adsorption; the wettability of extracted and UV/O$_3$ processed areas was also found to be similar (contact angle <20°).

In summary, we have demonstrated the formation of tricontinuous minimal surface mesophases in silica using the lipidic SDA glycerol monooleate. In addition to providing a route to mesostructured films with double gyroid symmetry, GMO is unusual in templating large (about 8 nm) pores in silica films after removal by UV/O$_3$ treatment or acid extraction; these large-pore films have a mixed gyroid/body centered nanostructure, with the latter tentatively assigned to a minimal surface phase on the basis of the I-WP geometry. When CTAB is used as a cosurfactant, the pore size distribution is dependent on the method of GMO removal, enabling macroscale patterning of pore size across the film. Future investigations will characterize the mesophase morphology of GMO/silica films in more detail, refining the structural assignment of the Im3m phase as well as testing our hypothesized mechanism for the origin of the larger than expected pore size and pore size dependence on the film processing procedure (collapse of the asymmetric I-WP structure). Further exploration of the GMO/silica phase space, varying the lipid to silica ratio, type of cosurfactant, or cosurfactant to GMO ratio, should yield other types of nanostructure morphologies, including the "double diamond" Pn3m tricontinuous structure. GMO may also find use as a biocompatible SDA, templating silica films while interfacing the resulting nanostructure with living cells using cell-directed assembly (CDA).[27,28]

Although phosphatidylcholine lipids have been investigated for this purpose,[13] strong interactions between phospholipid headgroups and silica were found to complicate the formation of a nanoporous silica matrix, an issue not present with the glycerol functionality of GMO.

■ METHODS

In a typical GMO/silica film synthesis, 25 mg of GMO was added to 0.6 mL of ethanol, 0.122 mL of tetraethylorthosilicate (TEOS), and 0.16 mL of 0.05 M HCl. After aging for 5 min, films were spin-coated at 2000 rpm at 15−20% relative humidity. Template removal was by UV/O$_3$ processing for 30 min in a UVO Model 42 ozone cleaner or by extraction for 10 s in 0.1 M HCl in ethanol.

GISAXS measurements were performed on beamline 8-ID at the Advanced Photon Source at Argonne National Laboratories using a wavelength of 1.6868 Å, a sample-to-detector distance of 1200 mm, and a 2048 × 2048 Marr CCD detector. Reflectivity measurements were used to position the sample angle in the range above the critical angle of the film but below that of the substrate, which is the criterion for grazing incidence; typical analysis angles were 0.18−0.20°. NANOCELL, a program developed at Purdue University for analysis of SAXS and GISAXS data of nanostructured materials, was used to fit the resulting 2-D scattering data.[15]

Nitrogen adsorption isotherms were collected using an in-house designed 96 MHz surface acoustic wave (SAW) apparatus interfaced with a Micromeritics ASAP 2020 surface area and porosimetry analyzer. TEM was performed on a JEOL 2010, operating at an accelerating voltage of 200 kV and equipped with a Gatan slow scan CCD camera. TEM samples were prepared by scraping the film with a sharp blade and transferring the flakes to a carbon-coated copper grid. Imaging was performed in under-focus conditions. AFM analysis was done on an Asylum MP3D BioAFM in noncontact mode using a SuperSharpSilicon cantilever (Nanoworld, typical tip radius = 2 nm). Images were taken at 512 × 1024 resolution, flattened using a third-order polynomial method, and filtered using a 5 × 5 Gian filter. Fluorescence microscopy images were acquired using standard FITC and TRITC filter sets (Semrock) on a Nikon Eclipse Ti inverted microscope with a 4X objective and equipped with an iXon 885 EMCCD camera. Image analysis was performed using Image J. The IW-P surface of Figure 4 was generated using Surface Evolver.[29]

■ ASSOCIATED CONTENT

Ⓢ **Supporting Information.** Further GISAXS and AFM data. This material is available free of charge via the Internet at http://pubs.acs.org.

■ AUTHOR INFORMATION

Corresponding Author
*E-mail: cjbrink@sandia.gov.

Present Addresses
[⊥]NIST Polymers Division, NIST, Gaithersburg, Maryland 20899, United States.
[#]Dow Chemical Company, Midland, Michigan 48674, United States.

■ ACKNOWLEDGMENT

■ REFERENCES

(1) Sanchez, C.; Boissiere, C.; Grosso, D.; Laberty, C.; Nicole, L. *Chem. Mater.* **2008**, *20*, 682–737.

(2) Lu, Y. F.; Ganguli, R.; Drewien, C. A.; Anderson, M. T.; Brinker, C. J.; Gong, W. L.; Guo, Y. X.; Soyez, H.; Dunn, B.; Huang, M. H.; Zink, J. I. *Nature* **1997**, *389* (6649), 364.

(3) Kresge, C. T.; Leonowicz, M. E.; Roth, W. J.; Vartuli, J. C.; Beck, J. S. *Nature* **1992**, *359* (6397), 710.

(4) Wei, T. C.; Hillhouse, H. W. *Langmuir* **2007**, *23* (10), 5689–5699.

(5) Crossland, E. J. W.; Kamperman, M.; Nedelcu, M.; Ducati, C.; Wiesner, U.; Smilgies, D. M.; Toombes, G. E. S.; Hillmyer, M. A.; Ludwigs, S.; Steiner, U.; Snaith, H. J. *Nano Lett.* **2008**, *9* (8), 2807.

(6) Khlebnikov, S.; Hillhouse, H. W. *Phys. Rev. B* **2009**, *80* (11), 115316.

(7) Hayward, R. C.; Alberius, P. C. A.; Kramer, E. J.; Chmelka, B. F. *Langmuir* **2004**, *20*, 5998–6004.

(8) Urade, V. N.; Wei, T.-C.; Tate, M. P.; Kowalski, J. D.; Hillhouse, H. W. *Chem. Mater.* **2007**, *19* (4), 768–777.

(9) Crossland, E. J. W.; Kamperman, M.; Nedelcu, M.; Ducati, C.; Wiesner, U.; Smilgies, D. M.; Toombes, G. E. S.; Hillmyer, M. A.; Ludwigs, S.; Steiner, U.; Snaith, H. J. *Nano Lett.* **2009**, *9* (8), 2807.

(10) Tate, M. P.; Urade, V. N.; Gaik, S. J.; Muzzillo, C. P.; Hillhouse, H. W. *Langmuir* **2010**, *26* (6), 4357–4367.

(11) Qiu, H.; Caffrey, M. *Biomaterials* **2000**, *21*, 223–234.

(12) Cherezov, V.; Clogston, J.; Misquitta, Y.; Abdel-Gawad, W.; Caffrey, M. *Biophys. J.* **2002**, *83*, 3393–3407.

(13) Dunphy, D. R.; Alam, T. M.; Tate, M. P.; Hillhouse, H. W.; Smarsly, B.; Collord, A. D.; Carnes, E.; Baca, H. K.; Kohn, R.; Sprung, M.; Wang, J.; Brinker, C. J. *Langmuir* **2009**, *25* (16), 9500–9509.

(14) Dunphy, D. R.; Garcia, F. L.; Jiang, Z.; Strzalka, J.; Wang, J.; Brinker, C. J. *Chem Commun.* **2011**, *47*, 1806–1808.

(15) Tate, M. P.; Urade, V. N.; Kowalski, J. D.; Wei, T.; Hamilton, B. D.; Eggiman, B. W.; Hillhouse, H. W. *J. Phys. Chem. B* **2006**, *110*, 9882–9892.

(16) Jiang, Z.; Lin, X. M.; Sprung, M.; Narayanan, S.; Wang, J. *Nano Lett.* **2010**, *10* (3), 799–803.

(17) Toombes, G. E. S.; Finnefrock, A. C.; Tate, M. W.; Ulrich, R.; Wiesner, U.; Gruner, S. M. *Macromolecules* **2007**, *40* (25), 8974–8982.

(18) Dattelbaum, A. M.; Amweg, M. L.; Ruiz, J. D.; Ecke, L. E.; Shreve, A. P.; Parikh, A. N. *J. Phys. Chem. B* **2005**, *109* (30), 14551–14556.

(19) Urade, V.; Hillhouse, H. *J. Phys. Chem. B* **2005**, *109*, 10538–10541.

(20) Ricco, A. J.; Frye, G. C.; Martin, S. J. *Langmuir* **1989**, *5*, 273–276.

(21) Jaroniec, M.; Kruk, M.; Olivier, J. P.; Koch, S. In *A New Method for the Accurate Pore Size Analysis of Mcm−41 and Other Silica-Based Mesoporous Materials*, Fifth International Symposium on the Characterization of Porous Solids, COPS V, Heidelburg, 1999; Unger, K. K., Kreysa, G., Baselt, J. P., Eds.; Elsevier: Heidelburg, 1999; pp 71−80.

(22) Choma, J.; Jaroniec, M.; Burakiewicz-Mortkaa, W.; Kloskea, M. *Appl. Surf. Sci.* **2002**, *196* (1−4), 216–223.

(23) Brezesinski, T.; Erpen, C.; Iimura, K.; Smarsly, B. *Chem. Mater.* **2005**, *17* (7), 1683–1690.

(24) Chan, V. Z. H.; Hoffman, J.; Lee, V. Y.; Iatrou, H.; Avgeropoulos, A.; Hadjichristidis, N.; Miller, R. D.; Thomas, E. L. *Science* **1999**, *286* (5445), 1716–1719.

(25) Sakamoto, Y.; Kaneda, M.; Terasaki, O.; Zhao, D. Y.; Kim, J. M.; Stucky, G.; Shim, H. J.; Ryoo, R. *Nature* **2000**, *408* (6811), 449–453.

(26) Doshi, D. A.; Huesing, N. K.; Lu, M.; Fan, H.; Lu, Y.; Simmons-Potter, K.; Potter, B. G., Jr.; Hurd, A. J.; Brinker, C. J. *Science* **2000**, *290* (5489), 107–111.

(27) Carnes, E. C.; Lopez, D. M.; Donegan, N. P.; Cheung, A.; Gresham, H.; Timmins, G. S.; Brinker, C. J. *Nat. Chem. Biol.* **2010**, *6* (1), 41–45.

(28) Baca, H. K.; Ashley, C.; Carnes, E.; Lopez, D.; Flemming, J.; Dunphy, D.; Singh, S.; Chen, Z.; Liu, N.; Fan, H.; Lopez, G. P.; Brozik, S. M.; Werner-Washburne, M.; Brinker, C. J. *Science* **2006**, *313*, 337–341.

(29) Brakke, K. A. *Exp. Math.* **1992**, *1* (2), 141–165.